Moesin and cortactin control actin-dependent multivesicular endosome biogenesis

Olivia Muriel, Alejandra Tomas[†], Cameron C. Scott, and Jean Gruenberg*
Department of Biochemistry, University of Geneva, 1211 Geneva 4, Switzerland

ABSTRACT We used in vivo and in vitro strategies to study the mechanisms of multivesicular endosome biogenesis. We found that, whereas annexinA2 and ARP2/3 mediate F-actin nucleation and branching, respectively, the ERM protein moesin supports the formation of F-actin networks on early endosomes. We also found that moesin plays no role during endocytosis and recycling to the plasma membrane but is absolutely required, much like actin, for early-to-late-endosome transport and multivesicular endosome formation. Both actin network formation in vitro and early-to-late endosome transport in vivo also depend on the F-actin–binding protein cortactin. Our data thus show that moesin and cortactin are necessary for formation of F-actin networks that mediate endosome biogenesis or maturation and transport through the degradative pathway. We propose that the primary function of endosomal F-actin is to control the membrane remodeling that accompanies endosome biogenesis. We also speculate that this mechanism helps segregate tubular and multivesicular membranes along the recycling and degradation pathways, respectively.

INTRODUCTION

In higher eukaryotic cells, solutes, ligands, and membrane components that have been endocytosed are delivered to common early endosomes. From there, some proteins and lipids are recycled back to the plasma membrane, whereas others are routed to the *trans*-Golgi network (TGN) or toward late endosomes and lysosomes for degradation (Huotari and Helenius, 2011; Scott *et al.*, 2014). The early endosome thus serves as an initial sorting nexus in the vacuolar apparatus that controls notably the reutilization versus degradation of membrane components.

In early endosomes, the sorting of protein along the recycling and degradation pathways is accompanied by major and concomi-

tant membrane remodeling and deformation processes. Retrograde transport to the TGN and recycling to the plasma membrane are mediated by membrane tubules, which form in a process that depends on the retromer, branched actin, and the WASP and SCAR homologue (WASH) complex (Puthenveedu *et al.*, 2010; Seaman *et al.*, 2013; Burd and Cullen, 2014). By contrast, activated signaling receptors and other molecules destined for late endosomes and lysosomes are incorporated into vesicular portions of the early endosome and sorted by endosomal sorting complexes required for transport (ESCRT) into luminal invaginations, which are pinched off as free cargo-containing intraluminal vesicles (ILVs; Woodman and Futter, 2008; Henne *et al.*, 2011; Scott *et al.*, 2014). These multivesicular regions expand and then detach or mature from early endosomes, becoming free multivesicular endosomal intermediates, referred to as endosomal carrier vesicles (ECVs) or multivesicular bodies (MVBs), which transport cargoes to late endosomes.

We previously reported that the biogenesis of ECV/MVBs requires polymerized actin nucleated on the early endosomal membrane via the lipid-binding protein annexinA2 (ANXA2; Emans *et al.*, 1993; Mayran *et al.*, 2003; Morel *et al.*, 2009). On the endosomal membrane, ANXA2 was found closely associated with small F-actin patches that also contained moesin (MSN; Harder *et al.*, 1997; Morel *et al.*, 2009; Puthenveedu *et al.*, 2010), a member of the ezrin, radixin, and moesin (ERM) family that may play a role in endosome maturation together with the homotypic fusion and protein sorting (HOPS) complex (Chirivino *et al.*, 2011). Actin also plays a role in

cargo transport toward lysosomes (Durrbach et al., 1996; Taunton et al., 2000; Morel et al., 2009) together with myosin 1B (Raposo et al., 1999; Taunton et al., 2000), which is also involved in the sorting of the protein cargo PMEL17 into multivesicular endosomes (Salas-Cortes et al., 2005).

Here we studied the mechanisms of actin-dependent endosome biogenesis along the degradative pathway using in vivo and in vitro strategies. We find that MSN is required for the formation of ECV/MVBs and for early-to-late endosome transport, as is the F-actin–binding protein cortactin (CTTN), and that MSN or CTTN depletion fully recapitulates the effects of actin depolymerization in vivo. We conclude that patches of F-actin discriminate the site of ECV/MVB formation on early endosome membranes and thus the membrane-remodeling process that accompanies endosome biogenesis.

RESULTS

Moesin is associated with early endosomes

Because MSN had been found in the vicinity of ANXA2-containing actin patches (Morel et al., 2009), we decided to analyze the intracellular distribution of MSN in more detail. By immunofluorescence, MSN showed a diffuse cytosolic pattern with puncta as well as plasma membrane labeling (Bonilha et al., 1999). Cells were therefore prepermeabilized to reduce the contribution of the cytosolic pool, and endosomes were enlarged by overexpression of the RAB5 dominant-active mutant Q79L to increase spatial resolution (Raiborg et al., 2002; Pons et al., 2008). Endogenous MSN was observed on enlarged endosomes, where it partially colocalized with ANXA2 (Figure 1A; background fluorescence is due to the permeabilization/fixation protocol necessary to visualize ANXA2). Similarly, MSN–green fluorescent protein (GFP) colocalized with F-actin on enlarged early endosomes (Supplemental Figure S1A), and GFP tagging did not affect MSN membrane association (Supplemental Figure S1B).

After subcellular fractionation, MSN copurified with early endosomes containing RAB5 and ANXA2 and not with late endosomes containing RAB7 (Figure 1B). When fractionation was repeated using cells expressing monomeric red fluorescent protein (mRFP)–RAB5 and MSN-GFP, individual early endosomes labeled with both markers were readily observed in the early endosomal fraction (Supplemental Figure S1C). Finally, we analyzed endogenous MSN distribution by immunogold labeling of cryosections (Figure 1, C and D, and Supplemental Figure S2). To label early endosomes, we incubated cells for 15 min at 37°C with an antibody against the extracellular domain of the epidermal growth factor (EGF) receptor (EGFR) coupled to gold (Tomas et al., 2015) and challenged them with EGF. MSN was observed on the membrane of endosomes containing endocytosed EGFR at a density similar to that observed on the plasma membrane (Figure 1, C and D; a gallery of additional micrographs is shown in Supplemental Figure S2; quantification in Figure 1E). Labeling was specific since the number of gold particles per micrometer was significantly lower on mitochondrial and nuclear membranes in the same samples (Figure 1E). Taken together, these data demonstrate that MSN, in addition to its known distribution to the plasma membrane, is also present on early endosomes.

Moesin is unevenly distributed on endosomal membranes

Close inspection of the micrographs showed that MSN staining on early endosomes in vivo (Figure 1A) did not completely overlap with RAB5, consistent with the notion that early endosomes contain different membrane regions or domains (Gruenberg, 2001; Miaczynska and Zerial, 2002). To gain better insight into MSN distribution, we
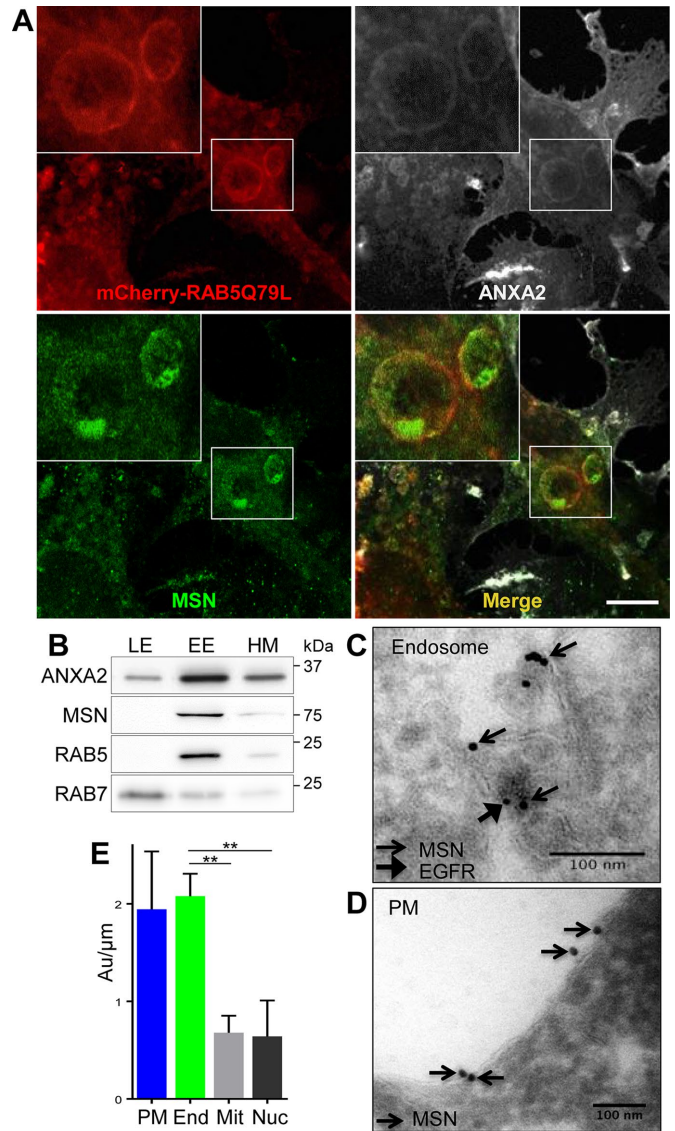

FIGURE 1: Localization of moesin to early endosomes. (A) BHK cells were transfected with mCherry-RAB5Q79L. After 24 h, they were prepermeabilized and processed for immunofluorescence with antibodies against MSN (green) and ANXA2 (gray) followed by secondary antibodies and analyzed by confocal fluorescence microscopy. Bar, 10 μm. (B) BHK cells were fractionated by flotation in gradients. Early endosomes (EE), late endosomes (LE), and heavy membranes (HM) were collected and analyzed by SDS–PAGE and Western blotting using antibodies against ANXA2, MSN, RAB5, and RAB7. Molecular weight (MW) markers are indicated. (C, D) HeLa cells were incubated with anti-EGFR antibody coupled to colloidal gold (6–8 nm, large arrow) and challenged with EGF. Thawed cryosections were prepared and labeled with anti-MSN antibody followed by Protein A–gold (10 nm; small arrows). Bar, 100 nm. (E) Quantification of the number of gold particles per linear micrometer in the experiments in C and D: plasma membrane (PM; 6 micrographs), endosomes (End; 13 micrographs), mitochondrial membrane (Mit; 6 micrographs), and nuclear envelope (Nuc; 5 micrographs). Data are means ± SEM. Endosomes vs. plasma membrane (ns, $p = 0.7983$), endosomes vs. mitochondria (**$p = 0.0012$), and endosomes vs. nucleus (**$p = 0.0072$). Micrographs were pooled from three different sections of a single labeling experiment from a gelatin-embedded cell pellet.

prepared early endosome fractions from cells expressing RAB5Q79L using the same protocol as used to prepare endosomes from cells expressing mRFP-RAB5 (Supplemental Figure S1C). Strikingly, Msn-GFP was not evenly distributed but concentrated locally on the limiting membrane of the enlarged endosomes, much like other endosomal machineries (Raiborg et al., 2002; Pons et al., 2008). Msn-GFP was indeed present in distinct patches that only partially colocalized with mRFP-RAB5Q79L (Supplemental Figure S3; quantification in Supplemental Figure S3, C–E) and occupied a smaller fraction of the endosome membrane than mRFP-RAB5Q79L (Supplemental Figure S3, D–E).

In line with these results, knockdown (KD) of ANXA2 had no effect on the endosome association of MSN, demonstrating that MSN membrane association is ANXA2 independent (Supplemental Figure S4A). Conversely, MSN KD had no effect on ANXA2 endosome association (Supplemental Figure S4A). Consistent with these observations, MSN did not copurify with ANXA2-GFP after ANXA2-GFP immunoprecipitation from purified early endosomes or after recombinant glutathione S-transferase (GST)–ANXA2 pull down, suggesting that the two proteins do not interact directly (Supplemental Figure S4, B and C). Next, given that MSN is an actin linker protein, we wondered whether endosome association was mediated by F-actin. However, excessive actin polymerization with jasplakinolide or depolymerization with cytochalasin D did not affect MSN recruitment to endosomes as analyzed by subcellular fractionation (Supplemental Figure S4D) and immunofluorescence (Supplemental Figure S4E). Taken together, these observations strongly suggest that MSN association to endosomes does not depend on actin and ANXA2. We thus wondered whether MSN interacted directly with lipids. Purified recombinant GST-MSN efficiently bound liposomes containing phosphatidylethanolamine (PE), cholesterol, and the negatively charged phospholipids phosphatidic acid (PA; Supplemental Figure S5A) and phosphatidylinositol (4,5)-bisphosphate (PIP2; Supplemental Figure S5B). No binding was observed when PA or PIP2 was replaced with phosphatidylcholine (PC; Supplemental Figure S5, A and B). Moreover, liposomes containing PIP2 could recruit full-length Msn-GFP from cytosolic extracts but not an N-terminal deletion mutant that lacks the FERM domain containing the PIP2-binding site (Supplemental Figure S5C), as expected (McClatchey, 2014). Taken together, these data show that MSN can bind negatively charged lipids, including PIP2, suggesting that these interactions may contribute to MSN recruitment onto endosomal membranes. Indeed, PIP2 may be present not only at the plasma membrane but also on intracellular membranes, including early endosomes (Tan et al., 2015). We conclude that MSN associates with specialized regions of early endosome membranes in a process that depends on negatively charged lipids but not on actin or ANXA2.

Moesin is required for early-to-late endosome transport

Because MSN is present in the early endosome, we investigated whether the protein is involved in endocytic trafficking. Depletion of MSN with small interfering RNAs (siRNAs) did not affect the internalization of transferrin (TF) receptor (TFR; Supplemental Figure S6A). Moreover, the bulk of endocytosed TF was returned to the medium within 20–30 min in cells lacking MSN, much like in control cells (Supplemental Figure S6A). These observations demonstrate that MSN is not involved in TFR internalization and recycling back to the plasma membrane. Similarly, after EGF challenge, MSN KD had no effect on EGFR internalization (Supplemental Figure S6A). Consistent with these observations, the appearance of endocytosed EGF-488 in early endosomes containing EEA1 during a 10-min incubation at 37°C was not affected by MSN depletion (Figure 2A), much like

the situation after ANXA2 depletion with siRNA (Figure 2A). These observations indicate that MSN is not directly involved in the trafficking of receptors between plasma membrane and early endosomes.

Next we investigated whether MSN played a role at a later step of the endocytic pathway. Cells treated with control siRNAs were incubated with EGF-488 for 10 min at 37°C as before and then chased for 50 min without EGF. The staining initially present at 10 min (Figure 2A) disappeared after the chase, presumably because the receptor/ligand couple had been transported to lysosomes and degraded (Figure 2A). By contrast, the EGF staining did not decrease upon chase in cells lacking MSN (Figure 2A), and EGF was retained in early endosomes containing EEA1 (Figure 2A). The retention of EGFR in EEA1-positive early endosomes was not due to some off-target effects of siRNAs, since the export from early endosomes was restored by the overexpression of mouse Msn (resistant to siRNAs against human MSN) in the MSN KD background (Supplemental Figure S6B; quantification in Supplemental Figure S6C).

Consistent with the observations that MSN plays a role in cargo export from early endosomes, EGFR degradation was significantly delayed upon MSN KD (Figure 2B; uncropped blots in Supplemental Figure S7, A–C; quantification in Figure 2C). However, EGFR degradation, much like export from early endosomes (Supplemental Figure S6, B and C), was partially restored after overexpression of RNA interference (RNAi)–resistant Msn in the MSN KD background (Figure 2B; uncropped blots in Supplemental Figure S7, A–C; quantification in Figure 2C). Msn overexpression itself had no effect in control cells and thus did not cause some gain-of-function phenotype (Figure 2, B and C; uncropped blots in Supplemental Figure S7, A–C). These observations demonstrate not only that the effects of anti-MSN siRNAs on EGFR degradation are specific and do not result from some off-target effects of the siRNAs, but also that GFP tagging does not interfere with Msn functions—hence, that GFP-Msn is fully active.

Finally, the siRNAs against MSN had no effect on the other two ERM family members, radixin and ezrin (Supplemental Figure S8A), and, conversely, the depletion of radixin or ezrin with siRNAs (Supplemental Figure S8, B and C) did not affect the degradation of EGFR (Supplemental Figure S8D). Taken together, these observations indicate that MSN, but not radixin or ezrin, is necessary for cargo transport or endosome maturation beyond early endosomes toward late endosomes and lysosomes.

The depletion of ANXA2 with siRNAs caused EGF retention in early endosomes (Figure 2A) and delayed EGFR degradation (Figure 2D; uncropped blots in Supplemental Figure S7, D–G; quantification in Figure 2E), much like MSN depletion (Figure 2, A–E), demonstrating that ANXA2 KD fully recapitulated the effects of MSN KD. Moreover, no additive effects were observed after double KD of both MSN and ANXA2 (Figure 2, A, D, and E; uncropped blots in Supplemental Figure S7, D–G). Hence our observations indicate that MSN and ANXA2 regulate EGF receptor transport from early endosomes toward lysosomes and that both proteins likely function in the same molecular pathway.

Ultrastructural analysis of endosomes after MSN depletion

Because MSN is present on the early endosome and MSN KD delays EGFR release from these endosomes and its subsequent degradation, we analyzed the ultrastructure of endosomes after MSN KD to gain further insights into the precise role of MSN. In mock-treated controls, BSA-gold endocytosed for 15 min at 37°C was often observed within multivesicular structures that resemble the ECV/MVBs that mediate early-to-late endosome transport (Figure 3A and Supplemental Figure S9, A–F). By contrast, after the depletion of MSN
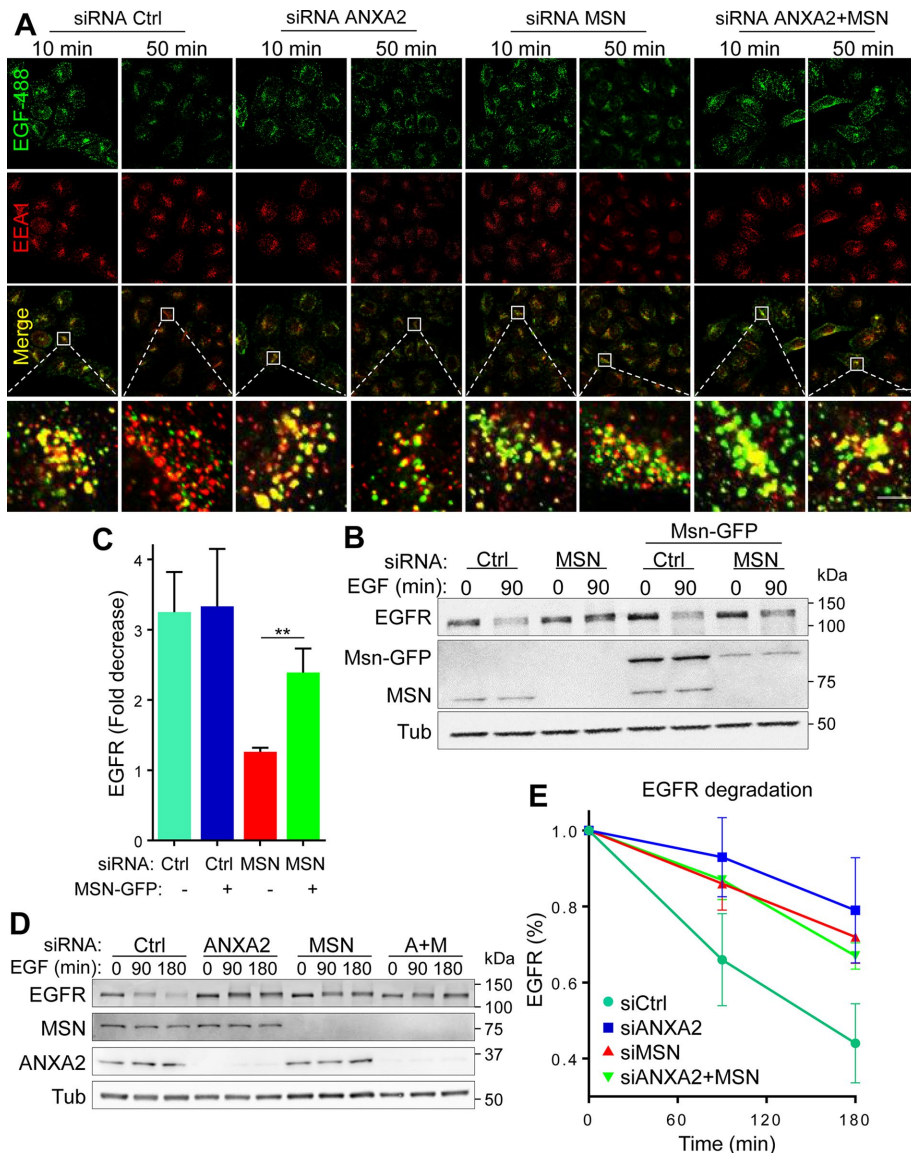
FIGURE 2: Moesin controls EGFR degradation. (A) HeLa cells were transfected with control siRNAs or siRNA to ANXA2 or MSN. Alternatively, they were double transfected with siRNAs to ANXA2 and MSN. Cells were treated for 1 h in serum-free medium, stimulated with 100 ng/μl EGF–Alexa 488 for 10 and 50 min, fixed, processed for immunofluorescence with an antibody against EEA1 followed by secondary antibody (red), and analyzed by fluorescence confocal microscopy. Bar, 25 μm (main images), 5 μm (insets). (B) HeLa cells were transfected with control (ctrl) siRNAs or siRNAs to MSN. Alternatively, they were double transfected with siRNAs (control or anti-MSN) and RNAi-resistant Msn-GFP, treated for 1 h in serum-free medium and 20 μg/ml cycloheximide, and stimulated or not with 100 ng/μl EGF for 90 min in the presence of 20 μg/ml cycloheximide. Cells were lysed and analyzed by SDS–PAGE and Western blotting using anti-EGFR antibody. γ-Tubulin (Tub) was used as a loading control. The uncropped versions of the same blots are shown in Supplemental Figure S7, A–C. MW markers are indicated. (C) Densitometric quantification of EGFR levels relative to tubulin from experiments as in B, using ImageJ software. Data are means of fold decrease at 90 min ± SEM ($n = 6$). siRNA control vs. siRNA MSN (**$p = 0.0059$), siRNA control vs. siRNA control + Msn-GFP (ns, $p = 0.9039$), siRNA control vs. siRNA MSN + Msn-GFP (ns, $p = 0.2273$), and siRNA MSN vs. siRNA MSN + Msn-GFP (**$p = 0.0081$). (D) HeLa cells were transfected with control siRNAs or siRNAs to ANXA2 or MSN or double transfected with siRNAs to both ANXA2 and MSN (A+M). Cells were then treated with EGF and analyzed as in B. The uncropped versions of the same blots are shown in Supplemental Figure S7, D–G. MW markers are indicated. (E) Densitometric quantification of the relative EGFR levels relative to tubulin from experiments as in A, using ImageJ software. Data are means ± SEM ($n = 3$). siRNA control vs. siRNA ANXA2 (90 min: $p = 0.00426$; 180 min: $p = 0.025$), siRNA control vs. siRNA MSN (90 min: $p = 0.0569$; 180 min: $p = 0.0111$) and siRNA control vs. siRNAs ANXA2 + Msn (90 min: $p = 0.0461$; 180 min: $p = 0.0166$).

with siRNAs, gold particles were mostly found in atypical ring-like structures connected to tubulocisternal elements reminiscent of the multivesicular region of early endosome rather than fully mature ECV/MVBs (Figure 3A and Supplemental Figure S9, G–L). Similar early endosome–like structures were also observed after ANXA2 KD (Mayran et al., 2003) and actin depolymerization (Morel et al., 2009). Again, no additive effects were observed after MSN and ANXA2 double KD (Figure 3A and Supplemental Figure S9, M–R). Interestingly, ILVs could still be observed in endosomes after MSN KD, demonstrating that delayed EGFR degradation cannot be accounted for by a defect in ILV formation. Our observations thus indicate that MSN does not play a role in the ESCRT-dependent sorting of EGFR into the ILVs of early endosomes but is necessary for the detachment of these multivesicular regions from early endosomes in order to become fully mature ECV/MVBs.

To better determine which endocytic step was affected by MSN KD, we labeled cells with the fluid-phase tracer horseradish peroxidase (HRP) endocytosed for 10 min at 37°C, followed by a 40-min chase in marker-free medium after depolymerization of the microtubules with nocodazole. Under these conditions, HRP leaves the early endosome but fails to reach late endosomes and remains in ECV/MVBs, which rely on polymerized microtubules for transport (Gruenberg et al., 1989; Aniento et al., 1993). In mock-treated controls, 80% HRP was indeed found in spherical multivesicular structures with the characteristic appearance of ECV/MVBs (Figure 3B and Supplemental Figure S10, A–G; quantification in Figure 3C). By contrast, the bulk of HRP (>70%) remained in tubular and ring-like structures resembling early endosomes after MSN and ANXA2 single or double KD (Figure 3B and Supplemental Figure S10, H–U; quantification in Figure 3C), consistent with our experiments after BSA-gold internalization (Figure 3A and Supplemental Figure S9). Taken together, these observations strongly suggest that MSN plays a crucial role in the full maturation program of ECV/MVB from early endosome membranes. We therefore conclude that MSN plays a direct role in the biogenesis or maturation of the ECV/MVB multivesicular intermediates that mediate cargo transport toward late endosomes.

Nucleation and polymerization of F-actin onto early endosomes in vitro

To gain insights into the role of MSN in the formation of F-actin patches on early endosome membranes, we used an in vitro assay
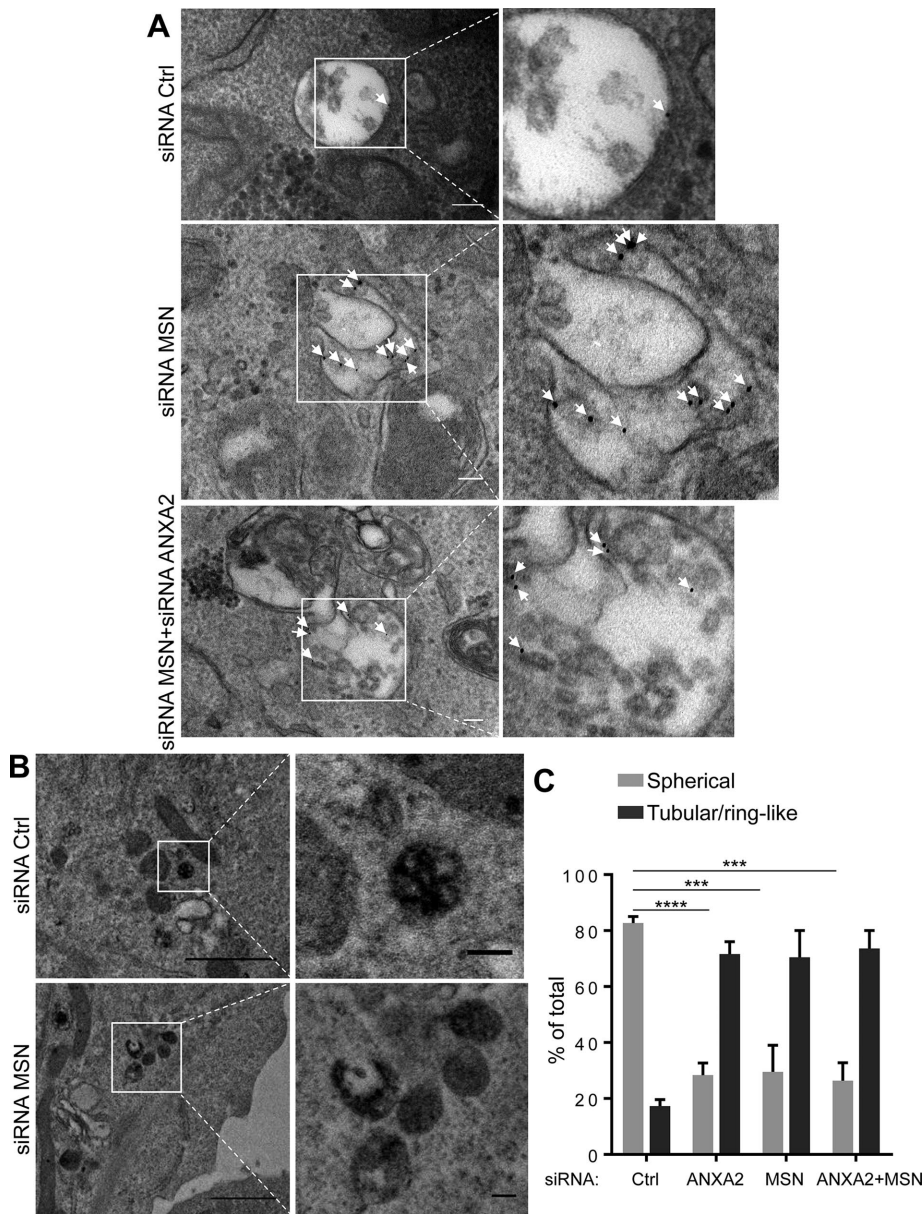
FIGURE 3: Endosome ultrastructure. (A) HeLa cells were transfected with control siRNA or siRNA to MSN or double transfected with siRNAs to MSN and ANXA2, and then treated for 1 h in serum-free medium. Cells were then incubated with BSA–gold (5 nm) ($OD_{520} = 5$) for 15 min at 37°C, fixed, and processed for electron microscopy. Arrows point at BSA–gold particles. Bars, 100 nm. (B) HeLa cells were transfected with control siRNAs or siRNAs to MSN. After microtubule depolymerization with 10 μM nocodazole for 2 h, HRP was endocytosed for 5 min followed by a 40-min chase, always in the presence of 10 μM nocodazole. Cells were processed for electron microscopy and HRP revealed using a cytochemical reaction (DAB). Bars, 1 μm (main images), 100 nm (insets). (C) Quantification of the percentage of HRP-containing endosomes with a tubular/ring-like morphology or spherical morphology from B. Data are means ± SD ($n = 3$). siRNA control vs. siRNA ANXA2 (****$p < 0.0001$), siRNA control vs. siRNA MSN (***$p = 0.0007$), and siRNA control vs. siRNAs ANXA2 + Msn (***$p = 0.0001$). Anx+Msn, ANXA2+Msn; Ctrl, control.

mRFP-RAB5 and Msn-GFP nucleated de novo actin polymerization selectively (Figure 4A), since no actin polymerization was detected when either the endosome or the cytosol was omitted (Supplemental Figure S11A). The actin nucleation and polymerization process was rapid, since F-actin could already be detected on some endosomes after 1 min (Supplemental Figure S11B). These short actin structures rapidly grew in length and became interconnected and branched, eventually forming a filamentous network (Figure 4B and Supplemental Figure S11B), presumably reflecting unbalanced actin dynamics in vitro. These observations demonstrate that early endosomes have the intrinsic and specific capacity to trigger actin nucleation and polymerization (Morel et al., 2009).

ANXA2 KD essentially abolished actin nucleation and subsequent polymerization (Figure 4B), consistent with the proposed role of ANXA2 in actin nucleation (Morel et al., 2009). By contrast, MSN KD did not seem to affect the capacity of endosomes to nucleate actin (Figure 4B). However, actin-containing structures, whether individual filaments or filament bundles, remained mostly isolated from each other after MSN KD (Figure 4B), and the formation of an interconnected and branched network was markedly reduced after 30 min (Figure 4, B and C; quantification in Figure 4D). These effects of MSN KD did not result from some mechanical perturbation of the sample, since they were fully recapitulated when the assay was carried out with purified rhodamine-labeled actin in glass-bottomed dishes so that structures could be imaged directly, in the absence of any perturbation (Supplemental Figure S11C). Moesin depletion inhibited the process selectively, since the formation of F-actin networks was fully restored by expression of RNAi-resistant Msn-GFP in the MSN KD background (Figure 4C and Supplemental Figure S11D; quantification in Figure 4D).

Moesin is required for the formation of endosomal F-actin networks in vitro

Because MSN seems to play a role in the formation of actin network in vitro, we analyzed the process at early time points, when actin-containing structures can still be discriminated. However, the history and the complexity of branched actin network formation are not easily studied. To quantify network complexity, we therefore counted the number of structures originating from each endosome (primary structures) and compared this number with the number of all other actin-based structures that could be identified in the networks and that did not originate from endosomes (other structures) (Figure 5A; quantification in Figure 5B). After MSN KD, much like in the controls, each endosome was able to nucleate one

that reconstitutes the polymerization of actin on purified early endosomes (Morel et al., 2009). In this assay, early endosomes purified from cells expressing GFP- or mRFP-RAB5 (as in Figure 1B and Supplemental Figure S1C) were incubated with cytosol as a source of actin and other factors. At the desired time, the assay mixture was fixed, sampled, and placed on a microscopic slide, and F-actin was visualized with phalloidin. In the assay, early endosomes containing
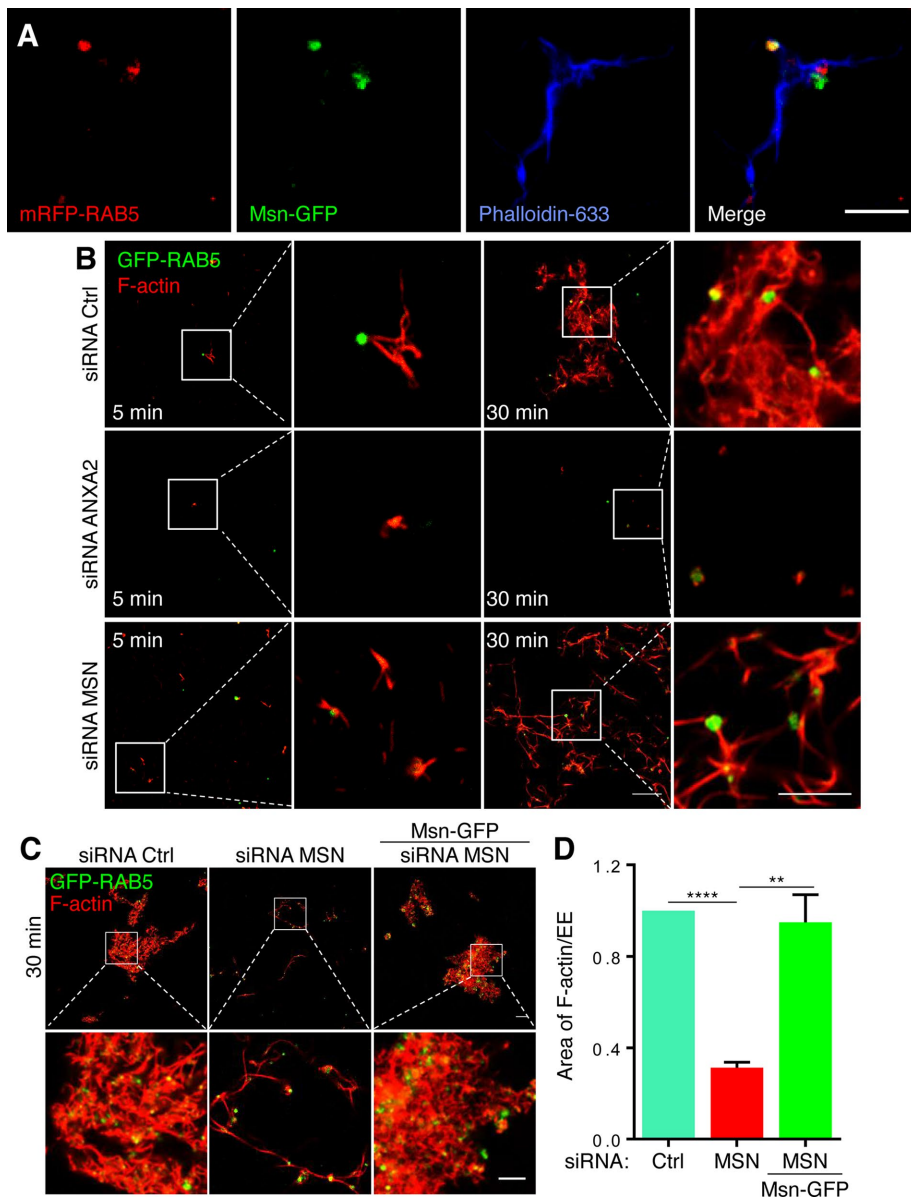
FIGURE 4: Nucleation and polymerization of F-actin on early endosomes in vitro. (A) BHK cells were transfected with mRFP-RAB5 and Msn-GFP. Cells were fractionated (as in Figure 1B), and early endosomes (EEs) were collected. In parallel, BHK cells were separately transfected with Msn-GFP as described, and cytosol was prepared. In the assay, EEs were mixed with cytosol, and the mixture was incubated for 7 min. The mixture was then fixed, labeled with phalloidin, and analyzed by fluorescence confocal microscopy. Bar, 5 μm. (B) The assay was as in A, except that EEs and cytosol were prepared from HeLa cells expressing GFP-RAB5 and transfected with control siRNAs or siRNA to ANXA2 or MSN. In the assay, EEs and cytosol were incubated for 5 or 30 min, and at the end of the reaction, the mixture was analyzed as in A. Bars, 10 μm (main images), 5 μm (insets). (C) The assay was as in B, except that EEs and cytosol were prepared from cells expressing GFP-RAB5 and transfected with control siRNA or siRNA against MSN. Alternatively, cells were cotransfected with siRNA against MSN and with an RNAi-resistant form of Msn-GFP (as in Figure 2B). Bar, 10 μm (main images), 5 μm (insets). The Western blots corresponding to these samples are shown in Supplemental Figure S6C. (D) Amounts of polymerized actin in C were quantified relative to the number of endosomes using the Cell Profiler software and were normalized to controls. Data are median ± SEM (n = 3). siRNA control vs. siRNA MSN (****p < 0.0001), siRNA control vs. siRNA MSN + Msn-GFP (ns, p = 0.6929), and siRNA MSN vs. siRNA MSN + Msn-GFP (**p = 0.0066).

ing that MSN depletion did not affect the actin nucleation capacity of early endosomes. However, in marked contrast to controls, few actin-based structures that did not originate from endosomes were observed after MSN KD (Figure 5A; quantification in Figure 5B). Note that the approximate length of individual actin-based structures was similar with or without MSN depletion both at early (Figure 5C) and late time points (Supplemental Figure S11F), perhaps suggesting that the observed decrease in complexity did not result from altered F-actin polymerization per se.

This reduced capacity to generate F-actin networks was reminiscent of defective F-actin branching capacity, a process that depends on the ARP2/3 complex (Pollard, 2007). Much like MSN KD, depletion of the p34ARP/APRC2 subunit of ARP2/3 complex with an siRNA pool (Supplemental Figure S12A) inhibited the formation of actin networks (Figure 5D), and most endosomes retained the capacity to nucleate F-actin (Supplemental Figure S11E). However, in contrast to MSN KD, the length of actin structures (Supplemental Figure S11F) and consequently the number of endosomes captured by actin structure (Figure 5E) were significantly increased by ARP2/3 depletion, presumably because branching is limiting during filament growth. Indeed, the effects of the double ARP2/3 and MSN KD were identical to the single ARP2/3 KD rather than MSN KD (Figure 5E and Supplemental Figures S11, E and F, and S12B). These data demonstrate that formation of actin networks on endosomes requires both functional MSN and the branching activity of ARP2/3 and that both MSN and Arp 2/3 act downstream of ANXA2, since the double MSN and ANXA2 KD or ARPC2 and ANXA2 KD were identical to the single ANXA2 KD (Supplemental Figure S12B).

Formation of F-actin networks in vivo

As a next step, we investigated whether MSN is also involved in the formation of F-actin patches or networks on early endosomes in vivo. To this end, we used CTTN, a well-established marker of branched actin networks (Cosen-Binker and Kapus, 2006; Derivery et al., 2009). After prepermeabilization to reduce the cytosolic pool, as in Figure 1A, CTTN showed a punctate staining pattern (Figure 6A) and colocalized with EEA1 on early endosomes (Figure 6A; quantification in Figure 6B), consistent with previous observations (Cabezas et al., 2005; Rosse et al., 2014). After depletion of ARPC2, the CTTN staining of early endosomes was essentially abolished, concomitant with an overall decrease in CTTN staining (Figure 6A; quantification in Figure 6B),
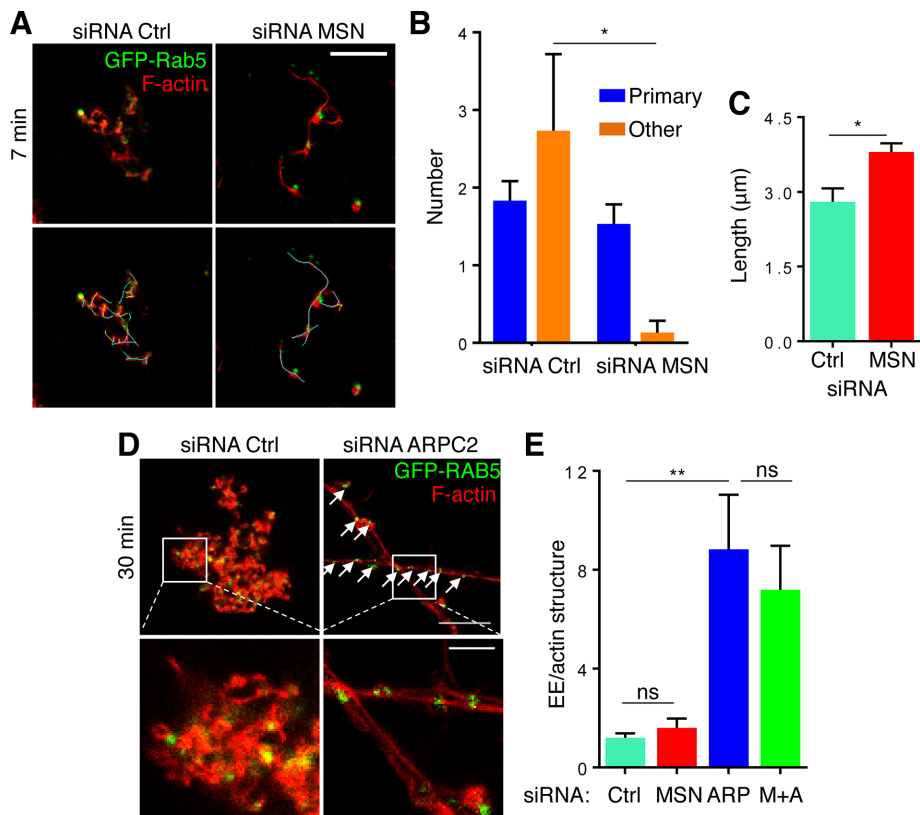
or two actin-based structures after a short incubation time (Figure 5A; blue bars in Figure 5B) and two or three actin-based structures at later time points (Supplemental Figure S11E), further demonstrat-

FIGURE 5: Moesin and endosomal F-actin networks in vitro. (A) Cells and cytosol were prepared as in Figure 4B after KD of MSN and the assay was carried out as in Figure 4B, except that samples were fixed after 7 min. Top and bottom, the same micrographs, but with structures overlaid with traces drawn using the NeuronJ plug-in of ImageJ at the bottom. Bar, 10 μm. (B) Quantification of the number of actin structures in A that originate (primary) or not (other) from endosomes. Data are means ± SD (*n* = 3). siRNA control vs. siRNA MSN (primary: ns, *p* = 0.2181; others: *p* = 0.0107). (C) The assay was as in A, and the length of actin structures was measured after 7 min. Data are means ± SEM (*n* = 3). *p* = 0.0354. (D) Cells and cytosol were prepared as in Figure 4B but after ARPC2 KD and the assay was carried out for 30 min as in Figure 4B. Bar, 10 μm (main images), 3 μm (insets). (E) The assay was as in Figure 4B using extracts from cells prepared after KD of MSN or ARPC2 (ARP) or double KD of MSN and ARPC2 (M+A). The number of endosomes per actin structure was quantified at 30 min. Data are means ± SEM (*n* = 5). siRNA control vs. siRNA MSN (ns, *p* = 0.3693), siRNA control vs. siRNA ARPC2 (**p* = 0.0088), siRNA MSN vs. siRNA ARPC2 (*p* = 0.0122), and siRNA ARPC2 vs. siRNAs MSN + ARPC2 (ns, *p* = 0.5792).

activates ARP2/3 and stabilizes actin branches after their formation (Uruno *et al.*, 2001; Weaver *et al.*, 2001). We therefore investigated whether CTTN functions in the same pathway as MSN. In our in vitro actin polymerization assay, GFP-CTTN was found on early endosomes labeled with mRFP-RAB5 (Figure 7A), as anticipated. Strikingly, CTTN depletion with siRNA abrogated actin network formation in a manner reminiscent of MSN KD (Figure 7B). We then investigated whether CTTN plays a role in endocytic membrane transport. CTTN KD did not affect TF binding to its receptor at the plasma membrane or TFR internalization and recycling (Supplemental Figure S13A). Similarly, EGF binding to EGFR at the plasma membrane and internalization into EEA1-labeled early endosomes for 15 min at 37°C were not affected by CTTN depletion (Figure 7C). These data demonstrate that CTTN does not play a role during endocytosis. By contrast, some EGF remained in early endosomes after a 45-min incubation time at 37°C in cells depleted of CTTN (Figure 7C), and EGFR degradation was significantly delayed (Figure 7D; quantification in Figure 7E), much like after MSN KD (Figure 2 and Supplemental Figures S6, B and C, and S7). Our data thus demonstrate that early-to-late endosome transport depends on F-actin networks polymerized onto early endosomes in a manner dependent on MSN and CTTN.

DISCUSSION
Actin plays a crucial role in membrane dynamics and intracellular transport in addition to its general roles in cell shape maintenance, adhesion, motility, and division (Clarke and Spudich, 1977; Mitchison and Cramer, 1996; Vale, 2003; Michelot and Drubin, 2011). In particular, phagocytosis and micropinocytosis are actin dependent, as are other endocytic processes (Soldati and Schliwa, 2006; Swanson, 2008; Mooren *et al.*, 2012), including the formation of clathrin-coated vesicles in yeast (Kaksonen *et al.*, 2005) and mammalian cells when the plasma membrane is under tension (Boulant *et al.*, 2011). In the endosomal system, actin plays a role along both the recycling (Huber *et al.*, 2000) and degradative pathways (Durrbach *et al.*, 1996; Taunton *et al.*, 2000) and in melanosome biogenesis (Salas-Cortes *et al.*, 2005). F-actin also plays a crucial role in the two major membrane deformation processes that occur on early endosome membranes—the formation of membrane tubules involved in retrograde transport and recycling (Seaman *et al.*, 2013) and the biogenesis of ECV/MVB (Morel *et al.*, 2009), which mediate transport toward late endosomes.

In previous studies, we found that ECV/MVB formation and detachment or maturation from early endosome membranes requires branched actin patches of short filaments nucleated by ANXA2 in a process that also depends on the actin nucleation factor Spire1 and ARP2/3 (Mayran *et al.*, 2003; Morel *et al.*, 2009). We also found that ANXA2 binds cholesterol-rich membranes, which seem to form

consistent with an extensive decrease in cellular branched actin. By contrast, MSN KD did not significantly affect total CTTN levels (Supplemental Figure S12C), but the association of CTTN with endosomes was drastically affected (Figure 6A; quantification in Figure 6B). As a control, WASH1 was depleted using siRNAs (Supplemental Figure S12D) in order to inactivate the WASH complex, an activator of ARP2/3 involved in retromer-dependent sorting and TFR recycling to the plasma membrane (Derivery *et al.*, 2009; Gomez and Billadeau, 2009). As expected, WASH1 KD also reduced CTTN recruitment to early endosomes (Figure 6A; quantification in Figure 6B). CTTN recruitment to early endosomes was significantly lower after double MSN and WASH1 KD compared with each single KD (Figure 6A; quantification in Figure 6B), suggesting that MSN and WASH act independently in recruiting CTTN and thus actin onto endosomes.

CTTN is required for the formation of endosomal F-actin networks
Our data indicate that CTTN is associated to endosomes in a MSN-dependent manner in vivo, whereas others have shown that CTTN
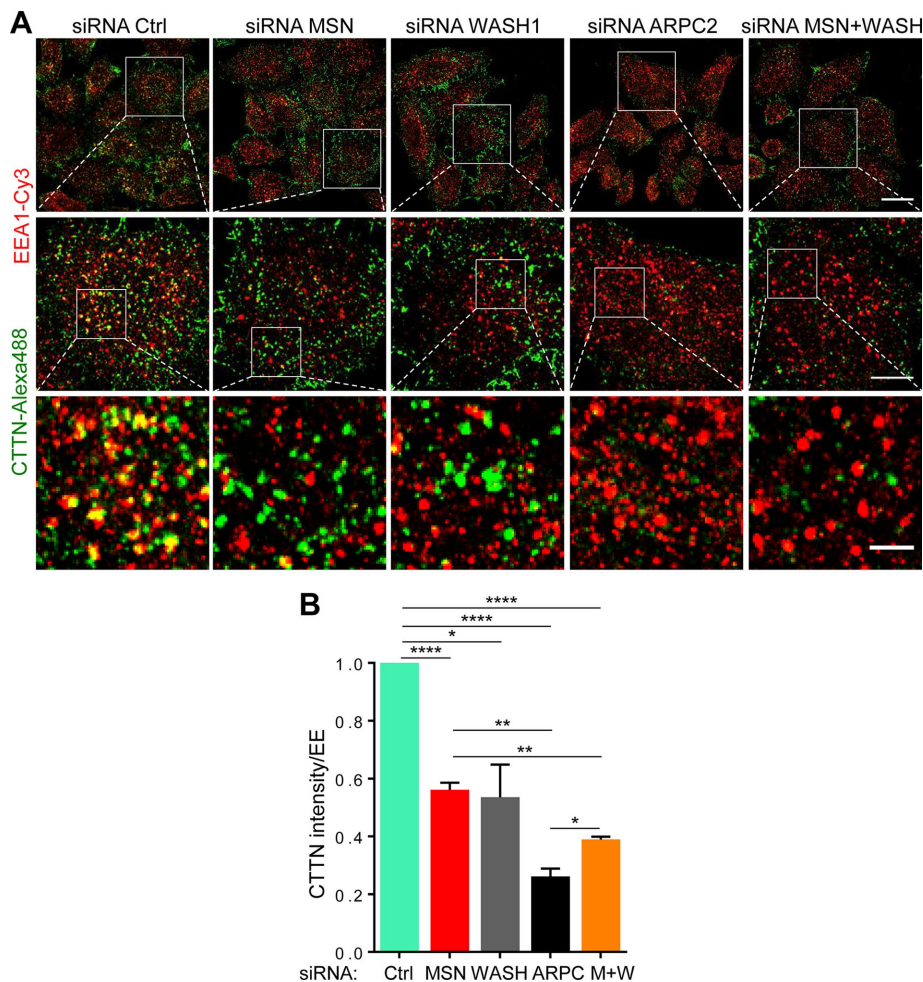
FIGURE 6: Recruitment of cortactin to early endosome in vivo. (A) HeLa cells transfected with control siRNAs or siRNAs to MSN, WASH1, or ARPC2 or double transfected with siRNAs to MSN and WASH1 were prepermeabilized (as in Figure 1A) and processed for immunofluorescence with antibodies against CTTN (green) and EEA1 (red). The upper row shows low magnification views (bar, 25 µm), and the indicated areas are shown at higher magnification in the middle row (bar, 10 µm). Similarly, the indicated areas in the middle row are shown at higher magnification in the lower row (bar, 3 µm). (B) The intensity of the CTTN staining was quantified per endosome labeled with EEA1 in A using the Cell Profiler software. ARPC, ARPC2; M+W, MSN and WASH1. Data are means ± SEM ($n = 3$). siRNA control vs. siRNA MSN (****$p < 0.0001$), siRNA control vs. siRNA WASH1 (*$p = 0.0146$), siRNA control vs. siRNA ARPC2 (****$p < 0.0001$), siRNA control vs. siRNAs MSN + WASH1 (****$p < 0.0001$), siRNA MSN vs. siRNA WASH1 (ns, $p = 0.8357$), siRNA MSN vs. siRNA ARPC2 (**$p = 0.0012$), siRNA MSN vs. siRNAs MSN + WASH1 (**$p = 0.0029$), and siRNA ARPC2 vs. siRNA MSN + WASH1 (*$p = 0.0111$).

been nucleated in an Anx2-dependent manner (see model in Supplemental Figure S13B). These filaments in turn can recruit the F-actin–binding protein CTTN, which may induce branched actin nucleation through ARP2/3 activation and stabilization of the branches (Uruno *et al.*, 2001; Goley and Welch, 2006; Hong *et al.*, 2015). Alternatively, CTTN may serve as a platform to scaffold nucleation-promoting factors and ARP2/3 to generate actin assembly in a process similar to adherens junctions in epithelial cells (Han *et al.*, 2014). In any case, CTTN contributes to the formation and stabilization of the branched actin network observed on endosomes, consistent with findings that CTTN and ARP2/3 regulate actin assembly on endosomes together with WASH (Puthenveedu *et al.*, 2010; Ohashi *et al.*, 2011; Monteiro *et al.*, 2013). This ANXA2-, MSN-, CTTN-, and ARP2/3-dependent process is absolutely required for transport beyond early endosomes, since interfering with any one of these components arrests the endosome maturation process and thus prevents downstream transport toward late endosomes and lysosomes and degradation.

One may envision that the primary role of endosomal F-actin is to deform the membrane mechanically in a process akin to endocytosis at the plasma membrane (Toret and Drubin, 2006). However, it is not clear how membrane-anchored F-actin could contribute to deform the membrane of relatively small (0.5–1 µm) and highly plastic endosomes. In addition, our ultrastructural analysis shows that MSN depletion does not prevent the membrane deformation process per se but hampers the separation of maturing ECV/MVBs (containing ILVs) from recycling membranes. It thus seems very attractive to conclude that the primary function of F-actin networks is to help segregate the tubular and multivesicular membranes of early endosomes along the recycling and degradation pathways, respectively (model in Supplemental Figure S13B). Once nucleated, presumably by ANXA2, F-actin filaments may be stabilized by WASH on nascent recycling tubules (Derivery *et al.*, 2009) and by MSN on nascent ECV/MVBs (this study). We conclude that patches of F-actin discriminate the site of ECV/MVBs formation on early endosome membranes and thus the membrane-remodeling process that accompanies endosome biogenesis.

MATERIALS AND METHODS

Cells, antibodies, and reagents

morphologically visible domains that may serve as actin nucleation/polymerization platforms (Harder *et al.*, 1997; Morel *et al.*, 2009) presumably corresponding to the membrane–actin contact sites we observe by light microscopy in this study. We now find that the assembly of F-actin patches on early endosome membranes, but not the actin nucleation process, depends on the ERM protein MSN. ERM proteins function as plasma membrane–cytoskeleton cross-linkers, coordinating signal transduction with cytoskeleton remodeling and membrane protein transport and activity (Tsukita and Yonemura, 1997; Bretscher *et al.*, 1997; Mangeat *et al.*, 1999; Bezanilla *et al.*, 2015). Increasing evidence indicates that ERM proteins are also involved in endocytic and phagocytic trafficking (Barroso-Gonzalez *et al.*, 2009; Chirivino *et al.*, 2011; Marion *et al.*, 2011).

It is thus very attractive to propose that the primary role of endosome-associated MSN is to capture the F-actin filaments that have
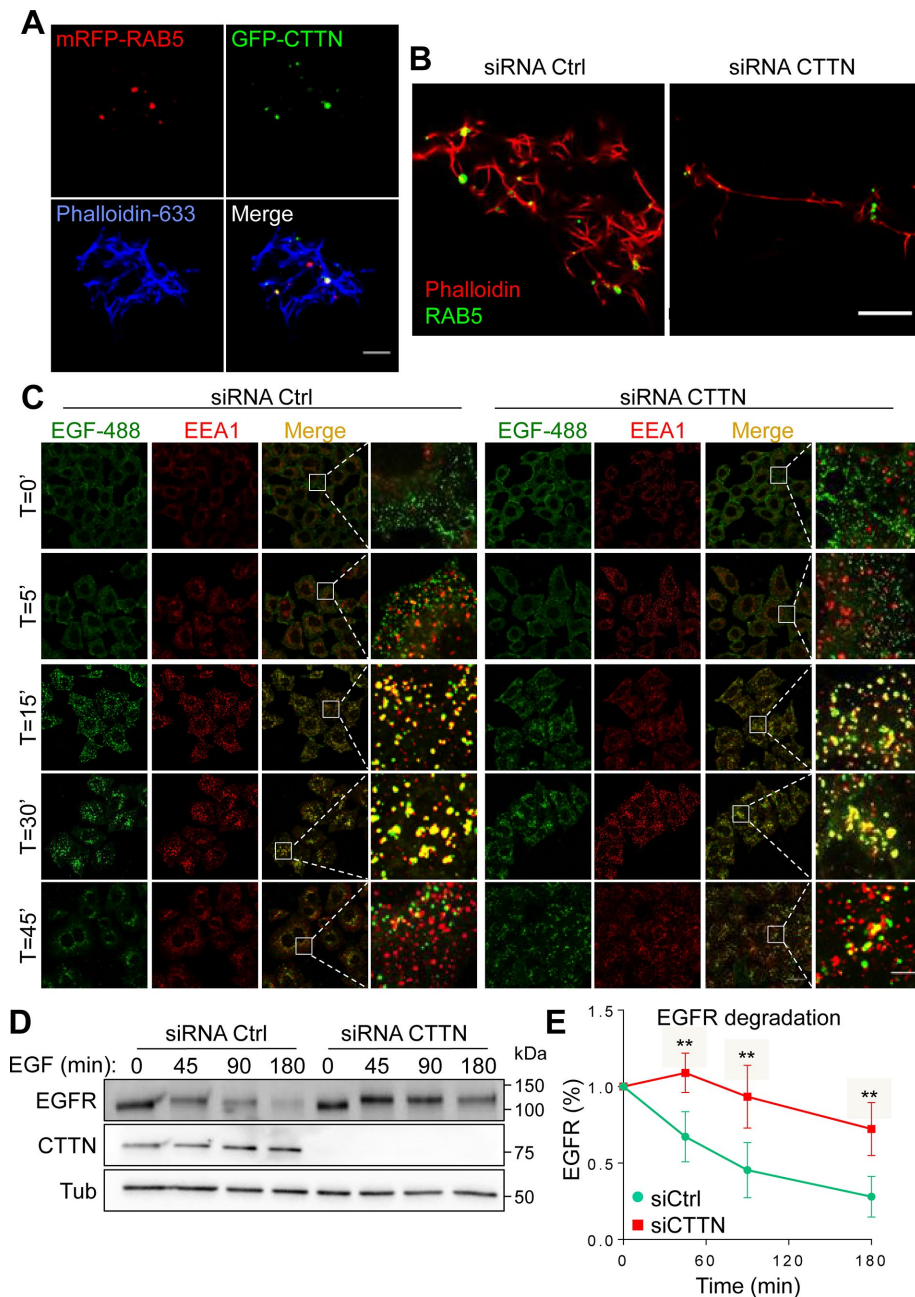
FIGURE 7: Cortactin and the formation of endosomal F-actin networks. (A) Endosomes were prepared from BHK cells transfected with mRFP-RAB5 and GFP-CTTN, whereas cytosol was prepared from cells transfected with GFP-CTTN only. The assay was as in Figure 4A. Bar, 5 μm. (B) Cells and cytosol were prepared as in Figure 4B after KD of CTTN with siRNAs. Assay was carried out as in Figure 4B. Bar, 10 μm. (C) HeLa cells transfected with control siRNAs or siRNAs to CTTN were treated for 1 h in serum-free medium and then incubated with 100 ng/μl EGF–Alexa 488 for 1 h at 4°C to allow binding to EGFR. After washing, cells were incubated at 37°C for the indicated times, fixed, labeled with an antibody against EEA1 followed by secondary antibody (red), and analyzed by fluorescence confocal microscopy. Scale bar, 25 μm (main images), 5 μm (zoom). (D) HeLa cells were transfected with control siRNAs or siRNAs to CTTN. Cells were treated for 1 h in serum-free medium and 20 μg/ml cycloheximide and stimulated or not with 100 ng/μl EGF for 45, 90, and 180 min in the presence of 20 μg/ml cycloheximide and lysed. Lysates were analyzed by SDS–PAGE and Western blotting using anti-EGFR antibody. γ-Tubulin (Tub) was used as a loading control. MW markers are indicated. (E) Densitometric quantification of EGFR levels relative to tubulin from D using ImageJ software. Data are means ± SD ($n = 5$). siRNA control vs. siRNA CTTN (45 min: **$p = 0.0021$; 90 min: **$p = 0.0043$; and 180 min: **$p = 0.0067$).

against RAB5 and ANXA2 (HH7) were gifts from R. Jahn (Max-Planck Institute for Biophysical Chemistry, Göttingen, Germany) and V. Gerke (University of Münster, Münster, Germany), respectively; the polyclonal antibodies against MSN and WASH1 were gifts from P. Mangeat (University of Montpellier II, Montpellier, France) and A. Gautreau (Ecole Polytechnique, Palaiseau, France), respectively. Mouse monoclonal antibodies were obtained from the following sources: EEA1 from Enzo (Lausanne, Switzerland); GFP from Roche (Mannheim, Germany); tubulin from Sigma-Aldrich (St. Louis, MO); cortactin from Millipore (Schaffhausen, Switzerland; clone 4F11); and EGFR from BD Biosciences (San Jose, CA). Rabbit monoclonal antibodies against actin, ezrin, radixin, or moesin (Cell Signaling, Danvers, MA) were from Cell Signaling. Rabbit polyclonal antibodies against WASH1 and RAB7 were from Sigma-Aldrich and against ARPC2 from Abcam (Cambridge, UK; p34Arc). Sheep antibody against human EGFR used for Western blot was from Fitzgerald (Acton, MA), peroxidase-conjugated secondary antibodies from Bio-Rad (Hercules, CA), and Cy2-, Cy3-, and Cy5-conjugated fluorescent antibodies from Jackson ImmunoResearch (West Grove, PA). Alexa Fluor 488–EGF and Alexa Fluor 555–TF were from Invitrogen. F-actin was labeled with Alexa Fluor coupled to phalloidin (Invitrogen). Latrunculin B, cytochalasin D, nocodazole, cycloheximide, and HRP were from Sigma-Aldrich, and jasplakinolide was from Calbiochem. Colloidal gold sols (British Biocell International) were coupled to anti-EGFR 108 antibody (raised against the extracellular domain of the receptor isolated from the mouse 108 hybridoma; American Type Culture Collection) or bovine serum albumin (BSA) by incubation with protein at pH 9.3 or 5.5, respectively, followed by secondary stabilization with 1% BSA as described (Slot and Geuze, 1985). Antibody–gold conjugate was diluted in serum-free medium containing 0.2% BSA and incubated with living cells. Lipids were obtained from Avanti Polar Lipids (Alabaster, AL). Purified rhodamine nonmuscle actin was obtained from Cytoskeleton (Denver, CO).

Plasmids and RNAi

We received plasmids from the following sources: GFP-RAB5 from M. Zerial (Max Planck Institute of Molecular Cell Biology and Genetics, Dresden, Germany); full-length Msn-GFP from P. Sánchez-Mateos (Complutense University School of Medicine,

Madrid, Spain; Estecha *et al.*, 2009) and C-MSN-GFP (C-terminal actin-binding region, amino acids 382–557) from H. Furthmayr (Stanford University, Palo Alto, CA; Amieva *et al.*, 1999), both tagged at the C-terminus; and ANXA2-GFP from V. Gerke (Münster, Germany). ANXA2-GFP was generated by cloning ANXA2 cDNA into pdsRED-monomer plasmid using *Xho* and *Bam*HI sites. CFP-RAB5 was generated by cloning RAB5 cDNA into pECFR-C1 plasmid using *Kpn*I and *Bam*HI sites. GFP-CTTN was generated using Gateway technology.

MSN was depleted using the ON-TARGETplus Human MSN (4478) siRNA SMARTpool, which includes the sequences CGTAT-GCTGTCCAGTCTAA; GAGGGAAGTTTGGTTCTTT; TCGCAAGCC-TGATACCATT; and GGCTGAAACTCAATAAGAA.

ANXA2 was depleted using the Qiagen siRNA Hs_ANXA2_10, CACGGCCTGAGCGTCCAGAAA, which was validated previously by reexpression of siRNA-resistant ANXA2 (Morel *et al.*, 2009).

We depleted p34Arc using the ON-TARGETplus human ARPC2 (10109) siRNA SMARTpool, which includes the sequences CCATG-TATGTTGAGTCTAA; GCTCTAAGGCCTATAUUCA; GGACAGAGT-CACAGTAGTC; and GTACGGGAGTTTCTTGGTA.

WASH1 was down-regulated using three different ON-TARGET-plus human WASH1 siRNAs: AGACCTATGCCGTGCCCTT; GTGCA-GGCCATTGGAGAGA; and AGACCTACAAGATGGGGTA.

Ezrin was down-regulated using the ON-TARGETplus Human EZR (7430) siRNA SMARTpool, which includes the sequences GCG-CAAGGAGGATGAAGTT; GGAAATCAACTATTTCGAGA; GCTCA-AAGATAATGCTATG and; GCGCGGAGCTGTCTAGTGA.

Radixin was down-regulated using the ON-TARGETplus Human RDX (5962) siRNA SMARTpool, which includes the sequences GGGCACAATTAGAGAATGA; CTACATGGCTTAAACTAAA; GGCA-TTAAGTTCAGAATTA; and GAGCTAATGGAACGTCTAA.

Cortactin was down-regulated using the ON-TARGETplus Human CTTN (2017) siRNA SMARTpool, which includes the sequences CCACGAAUAUCAGUCGAAA; GAACAAGACCGAAUGGAUA; GAGCAUAUCAACAUACACA; and CAAGUAACAUCAGAGCUAA. All target sequences are listed in the 5′-to-3′ direction.

In vivo experiments

To monitor EGFR endocytic transport, cells were starved overnight and preincubated for 1 h at 37°C with 20 μg/ml cyclohexamide in serum-free medium. The cells were then incubated for the indicated time periods at 37°C with 20 μg/ml cyclohexamide and 100 ng/ml EGF in DMEM containing 10 mM 4-(2-hydroxyethyl)-1-piperazineethanesulfonic acid (HEPES) at pH 7.4. Cells were lysed in RIPA buffer containing protease inhibitors, and the samples were analyzed by SDS gel electrophoresis, followed by Western blotting with antibodies against EGFR.

In vitro experiments

In our in vitro experiments, early and late endosome fractions, as well as heavy membranes, were prepared from cells expressing GFP-RAB5 by flotation in sucrose gradients using a well-established fractionation protocol (Aniento *et al.*, 1993). Briefly, after homogenization, a postnuclear supernatant was prepared adjusted to 40.6% sucrose in 3 mM imidazole, pH 7.4, loaded at the bottom of an ultracentrifuge tube, and overlaid sequentially with 35, 25, and 8.5% sucrose in the same buffer. After centrifugation, early and late endosomes were collected at the 35/25% and 25/8.5% interfaces, respectively, whereas heavy membranes were recovered at the load/35% interface. Fractions were then used in our in vitro actin polymerization assay or flash-frozen in liquid nitrogen and stored at –80°C.

In the actin polymerization assay (Morel *et al.*, 2009), purified GFP-RAB5 endosomes (final concentration ≈ 100 μg/ml) were mixed with HeLa cytosol (final concentration ≈ 1 mg/ml), 125 mM KCl, 20 mM HEPES (pH 7.0), 2.5 mM MgOAc2, 1.6 mM dithiothreitol, and a cocktail of protease inhibitors (Gruenberg *et al.*, 1989). Tubes were placed at 37°C without shaking. At the desired time, the assay mixture was sampled and placed on a microscopic slide. The reaction was stopped with 4% paraformaldehyde (PFA) on ice, polymerized actin was stained with Alexa Fluor 555 conjugated to phalloidin, and samples were analyzed by confocal microscopy. Alternatively, the assay was carried out in the absence of any mechanical perturbation. Microscopic chambers created by placing a 18-mm coverslip in a 35-mm dish with a 20-mm glass bottom (0.16–0.19 mm) were cleaned for 1 min with plasma cleaner, coated with 1% casein to minimize protein binding to the glass, and washed twice with 3 mM imidazole, pH 7.4. Actin polymerization was initiated by adding to the chamber the same assay mixture as described but also containing 0.1 μg/μl rhodamine-actin, and the final refraction index was adjusted with 39% sucrose and 3 mM imidazole, pH 7.4. Chambers were placed at 37°C without shaking, and images were acquired by confocal microscopy.

Electron microscopy

To study the ultrastructure of endosomes by electron microscopy, HeLa cells were preincubated or not for 2 h with 10 μM nocodazole in serum-free medium. Cells were then incubated for 5 min with 10 mg/ml HRP and 2 mg/ml BSA in DMEM containing 10 mM HEPES, pH 7.4, and further chased for 40 min at 37°C in the presence of 10 μM nocodazole. The cells were fixed for 1 h with 2% PFA and 2% glutaraldehyde in 0.1 M phosphate buffer at pH 7.4. The presence of HRP was revealed using 3,3′-diaminobenzidine (DAB) as substrate (Gruenberg *et al.*, 1989), and cells were flat-embedded and processed for transmission electron microscopy. Ultrathin 70-nm sections were stained with lead citrate and examined with a JEOL 1010 TEM, and images were acquired in a Gatan OriusSC100B charge-coupled device camera. Alternatively, cells were incubated with 5 nm BSA-gold (OD$_{520}$ ≈ 5) for 15 min at 37°C and then fixed and processed as described.

To monitor EGFR in endosomes, HeLa cells that had been serum starved were challenged with antibodies to the extracellular domain of EGFR bound to colloidal gold particles (6–8 nm) and 100 ng/ml EGF for 15 min at 37°C. Cells were fixed with 4% PFA and 0.1% glutaraldehyde in 0.1 M phosphate buffer at pH 7.4, scrapped off the dish, and pelleted in 12% gelatin. Subsequently, after infusion with 2.3 M sucrose, 80-nm sections were cut at 120°C and collected in 2.3 M sucrose/2% methylcellulose (1:1). The sections were immunolabeled with rabbit anti-moesin antibody at 1:5 dilution, followed by Protein A–gold (UMC Utrecht; size range 10–12 nm) as described previously (Slot *et al.*, 1991). The number of gold particles was quantified using ImageJ (National Institutes of Health, Bethesda, MD) and expressed per linear micrometer of plasma membrane and endosomes, as well as mitochondria and the nuclear membrane as controls.

Image analysis

To assess endosome association, fluorescence micrographs were processed using Cell Profiler (version 2.1.1; Kamentsky *et al.*, 2011). Endosomes were first identified as the primary object using the GFP-RAB5 (Figure 4) or EEA1 (Figure 6) signal, and the associated material was determined either by propagation of the secondary signal (actin; Figure 4) or by expanding the primary object (CTTN; Figure 6). Amounts of associated material for each object were averaged and normalized to the control condition.

The analysis of actin polymerization and network formation was performed using ImageJ. The length of actin structures,

number of endosomes per actin structure, and number of actin structures per endosome were quantified manually, and tracing and quantitation of actin network complexity was performed with the NeuronJ plug-in (Meijering et al., 2004). MSN distribution on early endosome membranes was also analyzed with ImageJ. The perimeter of the limiting membrane was traced, and the intensity profiles of both Msn-GFP and mCherry-RAB5Q79L were determined. A threshold of 20% of the maximum value for each channel was used to discriminate the distribution of patched versus nonpatched regions. The number of peaks was calculated manually. The percentage of coverage represents the fraction of the endosome perimeter occupied by protein. Density was estimated from the integral of the fluorescence intensity signal above threshold.

Biochemical methods

GST-MSN and GST-ANXA2 were produced in the BL21 bacteria strain. When indicated, the GST tag was removed by factor Xa cleavage and benzamidine treatment (Amersham Biosciences). The quality of recombinant protein was always assessed by SDS–PAGE, Coomassie blue staining, and Western blotting.

In GST pull downs, GST-ANXA2 or GST alone was incubated with glutathione-Sepharose beads (GE-Healthcare 4B) for 2 h at 4°C. Purified MSN was added, and the mixture was incubated for 2 h at 4°C. After sedimentation of the beads, bound and nonbound materials were analyzed by SDS–PAGE, Coomassie blue staining, and Western blotting.

To measure MSN binding, liposomes were prepared with the following compositions: PA:PE:cholesterol (2:2:1), PC:PE:cholesterol (2:2:1), PE:PC:cholesterol (2:2:1), PE:PC:cholesterol:PIP2 (2:1.5:1:0.5 or 1:1:1:2) after lipid hydration and sonication. Liposomes were incubated with purified GTS-MSN in 50 mM HEPES-NaOH, pH 7.4, containing 100 mM KCl for 90 min at room temperature. Alternatively, GST-MSN was replaced with cytosol prepared from cells overexpressing Msn-GFP (full length or mutant lacking FERM domain). The liposome-bound protein was separated from free protein by flotation in sucrose gradients. The liposome–protein mixture was adjusted to 40.6% sucrose, overlaid with 35% and 8.5% sucrose, and centrifuged for 1 h at 55,000 rpm. Fractions of the 8.5% interphase containing the liposomes, the 35% sucrose cushion, and the load were collected and analyzed by SDS–PAGE and Western blotting.

For immunoprecipitation, early endosomal fractions extracted from BHK cells transfected with ANXA2-GFP were diluted with twice-concentrated TNE buffer to a final concentration of 20 mM Tris, pH 7.4, 150 mM NaCl, 1 mM EDTA, 0.2% NP-40, and 10% glycerol in the presence of proteases inhibitors (aprotinin, leupeptin, and pepstatin). The endosomal extracts were then incubated with GFP-Trap_A beads (ChromoTek) under constant mixing for 1 h at 4°C. Beads were washed with TNE buffer containing 10% glycerol, resuspended in Laemmli buffer, and analyzed by SDS–PAGE and Western blotting.

The analysis of total membranes and cytosol was carried out by high-speed centrifugation of postnuclear supernatants (55,000 rpm for 50 min). Membranes and cytosol were recovered from the high-speed pellet and high-speed supernatant, respectively.

Other methods

The determination of protein concentration (Bradford, 1976) and SDS–PAGE (Laemmli, 1970) were described previously. Western blot was carried out by using WesternBright ECL (Advansta), and blot exposure times were always within the linear range of detection.

REFERENCES

Amieva MR, Litman P, Huang L, Ichimaru E, Furthmayr H (1999). Disruption of dynamic cell surface architecture of NIH3T3 fibroblasts by the N-terminal domains of moesin and ezrin: in vivo imaging with GFP fusion proteins. J Cell Sci 112, 111–125.

Aniento F, Emans N, Griffiths G, Gruenberg J (1993). Cytoplasmic dynein-dependent vesicular transport from early to late endosomes. J Cell Biol 123, 1373–1387.

Barroso-Gonzalez J, Machado JD, Garcia-Exposito L, Valenzuela-Fernandez A (2009). Moesin regulates the trafficking of nascent clathrin-coated vesicles. J Biol Chem 284, 2419–2434.

Bezanilla M, Gladfelter AS, Kovar DR, Lee WL (2015). Cytoskeletal dynamics: a view from the membrane. J Cell Biol 209, 329–337.

Bonilha VL, Finnemann SC, Rodriguez-Boulan E (1999). Ezrin promotes morphogenesis of apical microvilli and basal infoldings in retinal pigment epithelium. J Cell Biol 147, 1533–1548.

Boulant S, Kural C, Zeeh JC, Ubelmann F, Kirchhausen T (2011). Actin dynamics counteract membrane tension during clathrin-mediated endocytosis. Nat Cell Biol 13, 1124–1131.

Bradford MM (1976). A rapid and sensitive method for the quantitation of microgram quantities of protein utilizing the principle of protein-dye binding. Anal Biochem 72, 248–254.

Bretscher A, Reczek D, Berryman M (1997). Ezrin: a protein requiring conformational activation to link microfilaments to the plasma membrane in the assembly of cell surface structures. J Cell Sci 110, 3011–3018.

Burd C, Cullen PJ (2014). Retromer: a master conductor of endosome sorting. Cold Spring Harb Perspect Biol 6, a016774.

Cabezas A, Bache KG, Brech A, Stenmark H (2005). Alix regulates cortical actin and the spatial distribution of endosomes. J Cell Sci 118, 2625–2635.

Chirivino D, Del Maestro L, Formstecher E, Hupe P, Raposo G, Louvard D, Arpin M (2011). The ERM proteins interact with the HOPS complex to regulate the maturation of endosomes. Mol Biol Cell 22, 375–385.

Clarke M, Spudich JA (1977). Nonmuscle contractile proteins: the role of actin and myosin in cell motility and shape determination. Annu Rev Biochem 46, 797–822.

Cosen-Binker LI, Kapus A (2006). Cortactin: the gray eminence of the cytoskeleton. Physiology (Bethesda) 21, 352–361.

Derivery E, Sousa C, Gautier JJ, Lombard B, Loew D, Gautreau A (2009). The Arp2/3 activator WASH controls the fission of endosomes through a large multiprotein complex. Dev Cell 17, 712–723.

Durrbach A, Louvard D, Coudrier E (1996). Actin filaments facilitate two steps of endocytosis. J Cell Sci 109, 457–465.

Emans N, Gorvel JP, Walter C, Gerke V, Kellner R, Griffiths G, Gruenberg J (1993). Annexin II is a major component of fusogenic endosomal vesicles. J Cell Biol 120, 1357–1369.

Estecha A, Sanchez-Martin L, Puig-Kroger A, Bartolome RA, Teixido J, Samaniego R, Sanchez-Mateos P (2009). Moesin orchestrates cortical polarity of melanoma tumour cells to initiate 3D invasion. J Cell Sci 122, 3492–3501.

Goley ED, Welch MD (2006). The ARP2/3 complex: an actin nucleator comes of age. Nat Rev Mol Cell Biol 7, 713–726.

Gomez TS, Billadeau DD (2009). A FAM21-containing WASH complex regulates retromer-dependent sorting. Dev Cell 17, 699–711.

Gruenberg J (2001). The endocytic pathway: a mosaic of domains. Nat Rev Mol Cell Biol 2, 721–730.

Gruenberg J, Griffiths G, Howell KE (1989). Characterization of the early endosome and putative endocytic carrier vesicles in vivo and with an assay of vesicle fusion in vitro. J Cell Biol 108, 1301–1316.

Han SP, Gambin Y, Gomez GA, Verma S, Giles N, Michael M, Wu SK, Guo Z, Johnston W, Sierecki E, *et al.* (2014). Cortactin scaffolds Arp2/3 and WAVE2 at the epithelial zonula adherens. J Biol Chem 289, 7764–7775.

Harder T, Kellner R, Parton RG, Gruenberg J (1997). Specific release of membrane-bound annexin II and cortical cytoskeletal elements by sequestration of membrane cholesterol. Mol Biol Cell 8, 533–545.

Henne WM, Buchkovich NJ, Emr SD (2011). The ESCRT pathway. Dev Cell 21, 77–91.

Hong NH, Qi A, Weaver AM (2015). PI(3,5)P2 controls endosomal branched actin dynamics by regulating cortactin-actin interactions. J Cell Biol 210, 753–769.

Huber LA, Fialka I, Paiha K, Hunziker W, Sacks DB, Bahler M, Way M, Gagescu R, Gruenberg J (2000). Both calmodulin and the unconventional myosin Myr4 regulate membrane trafficking along the recycling pathway of MDCK cells. Traffic 1, 494–503.

Huotari J, Helenius A (2011). Endosome maturation. EMBO J 30, 3481–3500.

Kaksonen M, Toret CP, Drubin DG (2005). A modular design for the clathrin- and actin-mediated endocytosis machinery. Cell 123, 305–320.

Kamentsky L, Jones TR, Fraser A, Bray MA, Logan DJ, Madden KL, Ljosa V, Rueden C, Eliceiri KW, Carpenter AE (2011). Improved structure, function and compatibility for CellProfiler: modular high-throughput image analysis software. Bioinformatics 27, 1179–1180.

Laemmli UK (1970). Cleavage of structural proteins during the assembly of the head of bacteriophage T4. Nature 227, 680–685.

Mangeat P, Roy C, Martin M (1999). ERM proteins in cell adhesion and membrane dynamics. Trends Cell Biol 9, 187–192.

Marion S, Hoffmann E, Holzer D, Le Clainche C, Martin M, Sachse M, Ganeva I, Mangeat P, Griffiths G (2011). Ezrin promotes actin assembly at the phagosome membrane and regulates phago-lysosomal fusion. Traffic 12, 421–437.

Mayran N, Parton RG, Gruenberg J (2003). Annexin II regulates multivesicular endosome biogenesis in the degradation pathway of animal cells. EMBO J 22, 3242–3253.

McClatchey AI (2014). ERM proteins at a glance. J Cell Sci 127, 3199–3204.

Meijering E, Jacob M, Sarria JC, Steiner P, Hirling H, Unser M (2004). Design and validation of a tool for neurite tracing and analysis in fluorescence microscopy images. Cytometry A 58, 167–176.

Miaczynska M, Zerial M (2002). Mosaic organization of the endocytic pathway. Exp Cell Res 272, 8–14.

Michelot A, Drubin DG (2011). Building distinct actin filament networks in a common cytoplasm. Curr Biol 21, R560–R569.

Mitchison TJ, Cramer LP (1996). Actin-based cell motility and cell locomotion. Cell 84, 371–379.

Monteiro P, Rosse C, Castro-Castro A, Irondelle M, Lagoutte E, Paul-Gilloteaux P, Desnos C, Formstecher E, Darchen F, Perrais D, *et al.* (2013). Endosomal WASH and exocyst complexes control exocytosis of MT1-MMP at invadopodia. J Cell Biol 203, 1063–1079.

Mooren OL, Galletta BJ, Cooper JA (2012). Roles for actin assembly in endocytosis. Annu Rev Biochem 81, 661–686.

Morel E, Gruenberg J (2007). The p11/S100A10 light chain of annexin A2 is dispensable for annexin A2 association to endosomes and functions in endosomal transport. PLoS One 2, e1118.

Morel E, Parton RG, Gruenberg J (2009). Annexin A2-dependent polymerization of actin mediates endosome biogenesis. Dev Cell 16, 445–457.

Ohashi E, Tanabe K, Henmi Y, Mesaki K, Kobayashi Y, Takei K (2011). Receptor sorting within endosomal trafficking pathway is facilitated by dynamic actin filaments. PLoS One 6, e19942.

Pollard TD (2007). Regulation of actin filament assembly by Arp2/3 complex and formins. Annu Rev Biophys Biomol Struct 36, 451–477.

Pons V, Luyet PP, Morel E, Abrami L, van der Goot FG, Parton RG, Gruenberg J (2008). Hrs and SNX3 functions in sorting and membrane invagination within multivesicular bodies. PLoS Biol 6, e214.

Puthenveedu MA, Lauffer B, Temkin P, Vistein R, Carlton P, Thorn K, Taunton J, Weiner OD, Parton RG, von Zastrow M (2010). Sequence-dependent sorting of recycling proteins by actin-stabilized endosomal microdomains. Cell 143, 761–773.

Raiborg C, Bache KG, Gillooly DJ, Madshus IH, Stang E, Stenmark H (2002). Hrs sorts ubiquitinated proteins into clathrin-coated microdomains of early endosomes. Nat Cell Biol 4, 394–398.

Raposo G, Cordonnier MN, Tenza D, Menichi B, Durrbach A, Louvard D, Coudrier E (1999). Association of myosin I alpha with endosomes and lysosomes in mammalian cells. Mol Biol Cell 10, 1477–1494.

Rosse C, Lodillinsky C, Fuhrmann L, Nourieh M, Monteiro P, Irondelle M, Lagoutte E, Vacher S, Waharte F, Paul-Gilloteaux P, *et al.* (2014). Control of MT1-MMP transport by atypical PKC during breast-cancer progression. Proc Natl Acad Sci USA 111, E1872–E1879.

Salas-Cortes L, Ye F, Tenza D, Wilhelm C, Theos A, Louvard D, Raposo G, Coudrier E (2005). Myosin Ib modulates the morphology and the protein transport within multi-vesicular sorting endosomes. J Cell Sci 118, 4823–4832.

Scott CC, Vacca F, Gruenberg J (2014). Endosome maturation, transport and functions. Semin Cell Dev Biol 31, 2–10.

Seaman MN, Gautreau A, Billadeau DD (2013). Retromer-mediated endosomal protein sorting: all WASHed up. Trends Cell Biol 23, 522–528.

Slot JW, Geuze HJ (1985). A new method of preparing gold probes for multiple-labeling cytochemistry. Eur J Cell Biol 38, 87–93.

Slot JW, Geuze HJ, Gigengack S, Lienhard GE, James DE (1991). Immuno-localization of the insulin regulatable glucose transporter in brown adipose tissue of the rat. J Cell Biol 113, 123–135.

Soldati T, Schliwa M (2006). Powering membrane traffic in endocytosis and recycling. Nat Rev Mol Cell Biol 7, 897–908.

Swanson JA (2008). Shaping cups into phagosomes and macropinosomes. Nat Rev Mol Cell Biol 9, 639–649.

Tan X, Thapa N, Choi S, Anderson RA (2015). Emerging roles of PtdIns(4,5)P2–beyond the plasma membrane. J Cell Sci 128, 4047–4056.

Taunton J, Rowning BA, Coughlin ML, Wu M, Moon RT, Mitchison TJ, Larabell CA (2000). Actin-dependent propulsion of endosomes and lysosomes by recruitment of N-WASP. J Cell Biol 148, 519–530.

Tomas A, Vaughan SO, Burgoyne T, Sorkin A, Hartley JA, Hochhauser D, Futter CE (2015). WASH and Tsg101/ALIX-dependent diversion of stress-internalized EGFR from the canonical endocytic pathway. Nat Commun 6, 7324.

Toret CP, Drubin DG (2006). The budding yeast endocytic pathway. J Cell Sci 119, 4585–4587.

Tsukita S, Yonemura S (1997). ERM (ezrin/radixin/moesin) family: from cytoskeleton to signal transduction. Curr Opin Cell Biol 9, 70–75.

Uruno T, Liu J, Zhang P, Fan Y, Egile C, Li R, Mueller SC, Zhan X (2001). Activation of Arp2/3 complex-mediated actin polymerization by cortactin. Nat Cell Biol 3, 259–266.

Vale RD (2003). The molecular motor toolbox for intracellular transport. Cell 112, 467–480.

Weaver AM, Karginov AV, Kinley AW, Weed SA, Li Y, Parsons JT, Cooper JA (2001). Cortactin promotes and stabilizes Arp2/3-induced actin filament network formation. Curr Biol 11, 370–374.

Woodman PG, Futter CE (2008). Multivesicular bodies: co-ordinated progression to maturity. Curr Opin Cell Biol 20, 408–414.